JACS
JOURNAL OF THE AMERICAN CHEMICAL SOCIETY
pubs.acs.org/JACS
Article

Dynamics of Elementary Steps on Metal Surfaces at High Coverages: The Prevalence and Kinetic Competence of Contiguous Bare-Atom Ensembles

Wenshuo Hu and Enrique Iglesia*

Cite This: J. Am. Chem. Soc. 2024, 146, 22064−22076
Read Online

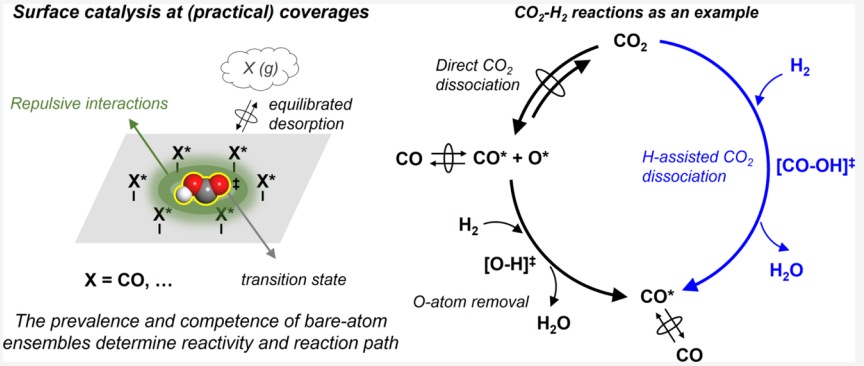

ABSTRACT: The rate of elementary steps on densely-covered surfaces depends sensitively on repulsive interactions within dense adlayers, situations ubiquitous in practice and with kinetic consequences seldom captured by Langmuirian treatments of surface catalysis. This study develops an ensemble-based method that assesses how such repulsion influences the prevalence and kinetic competence of bare-atom ensembles of different size. Chemisorbed CO (CO*) is used as an example because it forms dense adlayers on metal nanoparticles during CO_2 hydrogenation (CO_2−H_2) and other reactions, leading to significant repulsion that weakens the binding of CO* and kinetically-relevant transition states (TS). This approach is enabled by density functional theory and probability formalisms and describes the prevalence of ensembles of contiguous bare atoms from their formation energy (via CO* desorption); it then determines their competence in stabilizing the TS and mediating the reaction rates. The specific conclusions reflect the extent to which a given TS and CO* desorbed to form bare ensembles "sense" repulsion and the contribution of each ensemble size to each reaction channel mediated by distinct TS structures. These formalisms are illustrated by assessing the relative contributions, kinetic relevance, and ensemble size requirements for two CO_2−H_2 routes (direct and H-assisted CO_2 activation to CO and H_2O) on Ru nanoparticles, but they are not restricted to specific bound species or reaction channels. This method is essential to assess the kinetic relevance of elementary steps in a given catalytic sequence and to determine the contributions from parallel reaction channels at the crowded surfaces that prevail in the practice of surface catalysis.

1. INTRODUCTION

Surfaces are prevalently crowded under the conditions of their use as catalysts because high pressures and low temperatures provide the requisite kinetic driving force and energy efficiency for economic success. As a result, dense adlayers of reactants, intermediates, and products appear ubiquitously in the practice of catalysis;[1−6] these situations often preclude simple mechanistic descriptions, whether derived from theory or experiment. Bound species and, in particular, kinetically-relevant transition states (TS) bind at ensembles of bare surface sites that can form only by desorbing the most abundant species within these dense adlayers.[6−10] The binding of intermediates and transition states weakens through intermolecular repulsion imposed by the surrounding adlayers;[8−10] in such cases, it becomes increasingly more demanding (in terms of energy) to remove additional bound species to create even larger ensembles. The concomitant decrease in local coverages as "landing ensembles" form and grow relieves repulsion not only for the TS but also for vicinal adsorbed species. Consequently, as larger "landing ensembles" become more difficult to create, they also stabilize transition states more effectively, thus leading to the highest reaction rates on ensembles of intermediate size. The specific size of the

Received: June 8, 2024
Revised: July 12, 2024
Accepted: July 15, 2024
Published: July 29, 2024

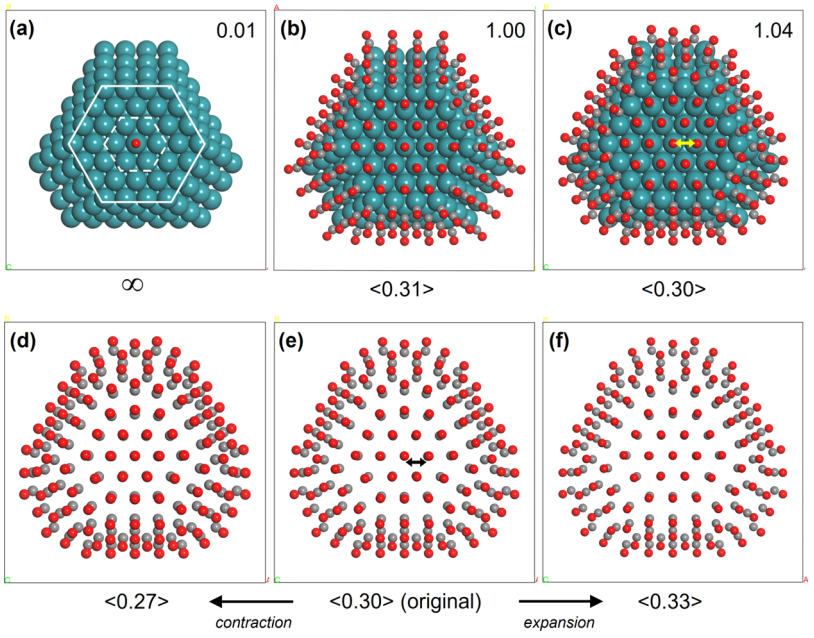

Figure 1. Hemispherical Ru_{218} nanoparticles at (a) 0.01, (b) 1.00, and (c) 1.04 ML of CO*. Lattice CO models with mean CO*−CO* distances ($\langle d_{CO} \rangle$, denoted in brackets and by arrows) of (d) 0.27, (e) 0.30, and (f) 0.33 nm. The solid hexagon in (a) indicates the (111) terrace; the dashed hexagon in (a) denotes terrace sites considered in this work to represent the terrace center region. Cyan: Ru, red: O, and gray: C.

most competent ensembles varies with temperature and adlayer density and differs among competing reaction channels and intermediates, with marked consequences for activity and selectivity in surface catalysis.

The accepted Langmuirian formalisms used to describe rates in surface catalysis seem to capture measured kinetic trends, even at high coverages, but only because the simple functional form of the resulting rate equations leads to regressed kinetic and thermodynamic parameters that describe rates well over the typical narrow range of pressures and temperatures.[7,11,12] Such treatments do not capture the effects of intermolecular interactions within dense adlayers or the kinetic relevance of diverse bare-site ensembles that can emerge from stochastic desorption events on crowded surfaces. Consequently, the values of the regressed parameters do not reflect the chemical meaning intended by the elementary steps used to derive the Langmuirian rate equations. Such matters are often neglected, in spite of their consequences for turnover rates and selectivity and the abundant evidence for their importance. Langmuirian formalisms represent convenient but incomplete descriptions of the chemical dynamics on densely-covered surfaces.

These challenges in describing and predicting reactivity (and selectivity) become most relevant and unavoidable in practice for reactions involving strongly-bound reactants, intermediates, spectators, or products. CO molecules, as reactants or products, represent one of the most frequent examples because they lead to high coverage of chemisorbed CO (CO*) on metal nanoparticles. High CO* coverages prevail at working conditions in Fischer−Tropsch synthesis (FTS),[13−16] water−-gas shift,[17,18] and CO_2 hydrogenation (CO_2−H_2)[19−22] catalysis, as well as in the removal of CO contaminants from either combustion effluents[2−4] or H_2 streams used in fuel cells.[23] These dense CO* adlayers and consequent CO*−CO* repulsion weaken CO* binding and destabilize the kinetically-relevant transition states (e.g., $[*HCOH*]^{‡}$ for FTS reactions). These effects lead to estimates of CO adsorption equilibrium constants (K_{CO}) and lumped rate parameters (e.g., the rate parameter in FTS turnover rates on Ru[9,10,24]) from kinetic trends that differ markedly from those derived from theory, kinetic measurements, or independent spectroscopic observations on less densely-covered surfaces.[4,10,25]

Such crowded surfaces are also relevant for CO_2−H_2 reactions, for which CO is a key intermediate and binds strongly on metal surfaces, leading to high CO* coverages.[19−22] Ru nanoparticle surfaces are nearly saturated with CO* in CO_2−H_2 reactions, even at low pressures (5−25 kPa CO_2, 8 kPa H_2, 573 K);[20] higher pressures that favor C−C coupling and the formation of methanol or larger hydrocarbon chains[21,26] lead to even denser CO* adlayers.

Accurate assessments of such repulsive interactions and their consequences for surface catalysis require a systematic theoretical analysis of the competence of each ensemble size in stabilizing the bound species and transition states. These effects have been previously considered using analytical methods, including quasi-chemical approximations (QCA)[27−29] and modified microkinetic models,[12,30−32] and by stochastic kinetic Monte Carlo (KMC) simulations[1,2,6,33,34] that implicitly or explicitly describe such intermolecular interactions. Here, we combine density functional theory (DFT) calculations with statistical derivations to account for the energy penalty incurred in desorbing contiguous bound species (with CO* as the illustrative case), which increases as ensembles grow and local coverages (and repulsion) decrease. These energy costs and the prevalent coverage throughout a nanoparticle combine to determine the probability of finding a landing ensemble of a given size. Their competence in stabilizing the kinetically-relevant TS then completes a description of the contributions of ensembles of any given size to turnover rates.

These formalisms address in a systematic manner how the TS and the most abundant bound species "sense", albeit to different extents, the repulsion imposed by coadsorbates based on their areal requirements and their specific interactions with the contiguous adlayers. These treatments enable explicit

https://doi.org/10.1021/jacs.4c07788
J. Am. Chem. Soc. 2024, 146, 22064−22076

elucidation of the consequences and chemical significance of such repulsive interactions for catalytic dynamics within thermodynamically quasi-equilibrated systems through the use of transition-state theory formalisms and analytical derivations of the prevalence of multisite ensembles of different sizes and shapes. These methods provide a structured analytical strategy for dissecting the dynamics of any elementary step on crowded surfaces into the probability of forming bare-site ensembles of a given size and their competence in stabilizing any given TS. They offer a strategic approach for examining the kinetic relevance of elementary steps in specific sequences and for assessing the relative contributions of parallel reaction channels on crowded surfaces that prevail in the practice of catalysis.

2. COMPUTATIONAL METHODS

Hemispherical Ru nanoparticles (218 Ru-atoms; Ru_{218}) were formed by excising them from Ru_{586} cuboctahedra (~2.5 nm in diameter) with CO* coverages of 0.01, 1.00, and 1.04 monolayer (ML, defined as the ratio of CO* molecules to surface Ru atoms) and removing bottom six layers along the (111) direction, as displayed in Figure 1a–c and detailed in previous works.[10,24] Supramonolayer CO* coverage (1.04 ML) was achieved by placing geminal dicarbonyl species on edge and corner Ru-atoms (Figure 1c).[24] Bound CO species on the 1.04 ML model have two binding configurations: linear atop CO* on a single Ru-atom (L-CO*; e.g., CO* bound at the terrace, Figure 1c) and CO* bridging two vicinal Ru-atoms (B-CO*; geminal dicarbonyl species on edge and corner Ru-atoms, Figure 1c). These two binding configurations have been detected in infrared spectra on dispersed Ru nanoparticles, showing bands at 1950–2050 cm^{-1} for L-CO* and at 1850–1950 cm^{-1} for B-CO*.[10,20] DFT-calculated CO* vibrational frequencies for the 1.04 ML model surfaces gave values of 1995 cm^{-1} for L-CO* species and 1878 cm^{-1} for B-CO* species,[10] consistent with the spectroscopic observations. Such particle structural models more accurately mimic actual metal nanoparticles and circumvent the unrealistic lateral rigidity imposed by periodic boundaries in extended slab models, thus allowing the presence of denser adlayers than those attainable on low-index surfaces.[4,7,10,24,25]

The inherent symmetry of Ru_{218} clusters allows only discrete changes in CO* coverages;[10,24] as a result, simplified CO lattice models[10] were also used to probe the effects of CO* adlayer density on its binding strength through monotonic contraction or expansion of the lattice. These models involve the extraction of CO* molecules from a 1.04 ML Ru_{218} nanoparticle at their equilibrium locations (denoted as the original lattice, Figure 1e) and then the variation of CO*–CO* distances by contracting or expanding the lattice to mimic interatomic distances prevalent at different CO* coverages and the consequences of repulsion. Three representative structures are depicted in Figure 1d–f. Such lattice models allow assessments of monotonic changes in intermolecular "discomfort", which cannot be determined from nanoparticle or periodic model structures.[10,35]

Periodic DFT calculations were performed using the *Vienna Ab-initio Simulation Package* (VASP)[36] and the revised Perdew–Burke–Ernzerhof (RPBE) functional.[37–39] Dispersive corrections by DFT-D3 with Becke and Johnson (BJ) damping[40,41] were used for the lattice models and all bound species (e.g., CO*, $[CO-O]^{\ddagger}$, $[CO-OH]^{\ddagger}$, $[O-H]^{\ddagger}$) on Ru_{218} nanoparticles. These corrections did not include Ru-atoms because of overpredictions of binding energies using D3 on Ru surfaces.[10,24] Projector augmented wave (PAW) treatments of core–valence interactions[42,43] were used with a plane wave cutoff of 400 eV. The first Brillouin zone was sampled at the Γ-point. The total energy was first converged to 10^{-4} eV and atomic forces to 0.05 eV/Å; they were then refined to 10^{-6} eV and 0.05 eV/Å in structure optimizations. The bottom two layers of Ru_{218} nanoparticles (and CO* molecules bound to them) were kept at their initial locations (determined by fully relaxing the original Ru_{586} cuboctahedra at three coverages) during structure optimizations and TS searches to prevent any structural rearrangement associated with the hemispherical nature of the model.[10,24] Lattice models at different CO*–CO* distances were optimized to 10^{-6} eV (total energy) and 0.05 eV/Å (atomic forces) by using the same RPBE functional and D3-BJ correction, with their O atoms relaxed and C-atoms fixed to preserve their close-packed structures. Such optimized locations were then kept fixed, and single-point calculations were performed to calculate CO* desorption from these lattice models. Functionals using generalized gradient approximation (GGA) may lead to CO "overbinding" on metal surfaces;[44] the RPBE functional used here provides more accurate CO binding energies than other GGA-type functionals like PBE and PW91.[39,45] More accurate calculations would require higher levels of theory (e.g., random phase approximation[44]), which cannot currently address the very large systems examined here (>2800 electrons for Ru_{218} nanoparticles[10]).

Vibrational frequencies were calculated by diagonalizing Hessian matrices derived from energy changes upon displacements (±0.015 Å) of each atom in the species involved in reactions and in spectator CO* bound to terrace sites (dashed hexagon; Figure 1a). These frequencies were used to calculate the zero-point vibrational energies (ZPE) and to derive enthalpies (H), entropies (S), and free energies (G) according to

$$H = E_0 + \mathrm{ZPE} + H_{\mathrm{trans}} + H_{\mathrm{rot}} + H_{\mathrm{vib}} \quad (1)$$

$$G = H - T(S_{\mathrm{trans}} + S_{\mathrm{rot}} + S_{\mathrm{vib}}) \quad (2)$$

where E_0 is the DFT-calculated electronic energy (with dispersive corrections). The subscripts "trans", "rot", and "vib" denote translational, rotational, and vibrational components of enthalpies and entropies derived from statistical mechanics formalisms.[46] Translations and rotations of strongly-bound species, such as CO* and transition states, were treated as vibrations.[10,24] Transition states were first isolated using nudged elastic band[47,48] methods with convergence criteria of 10^{-4} eV for total energies and 0.3 eV/Å for atomic forces. The Dimer[49] method was then used to refine the structure and energy of each TS to 10^{-6} eV and 0.05 eV/Å. Using tighter convergence criteria (e.g., 0.03 eV/Å) did not cause detectable changes in TS energies (<1 kJ mol^{-1}). Transition states were confirmed by the detection of one imaginary frequency corresponding to the vibration along the reaction coordinate.

3. RESULTS AND DISCUSSION

3.1. Treatments of Coverage-Dependent Binding on Curved and Crowded Surfaces. Langmuirian treatments describe equilibrium fractional coverages (θ_{CO*}) on surfaces in contact with fluid-phase CO molecules (CO pressure, [CO]) as

$$\theta_{CO*} = \frac{K_{CO}[CO]}{1 + K_{CO}[CO]} \quad (3)$$

where K_{CO} is the CO* binding constant, a function of the adsorption free energy (ΔG_{CO}; R is the gas constant, T is the temperature; free energies in this study are referenced to the standard state of 1 bar):

$$K_{CO} = \exp\left(-\frac{\Delta G_{CO}}{RT}\right) \quad (4)$$

In such formalisms, the probability of finding one unoccupied site (P_1) is

$$P_1 \equiv 1 - \theta_{CO*} = \frac{1}{1 + K_{CO}[CO]} \quad (5)$$

an expression that does not consider the occupation state of any adjacent sites. The probability of finding an *isolated* bare site (P_1^{iso}) imposes the additional requirement that all contiguous sites must be occupied by CO*:

https://doi.org/10.1021/jacs.4c07788
J. Am. Chem. Soc. 2024, 146, 22064–22076

Table 1. Values of Statistical Coefficient (ϕ_i) for Bare-Site Ensembles on Infinite hcp Surfaces

Ensemble size (i)	Ensemble shape (boundaries labelled by dotted polygons)		ϕ_i
2	pair		3
3	equilateral triangle	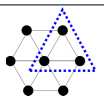	2
4	parallelogram	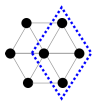	3
5	isosceles trapezoid	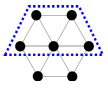	6
6	hexagon	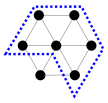	6

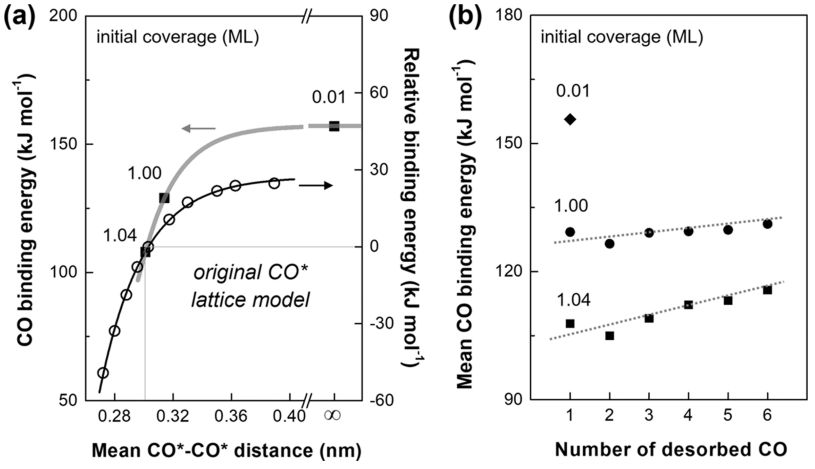

Figure 2. (a) DFT-derived CO* binding energy (ΔE_{CO}, eq 9) on Ru_{218} nanoparticles at 0.01, 1.00, and 1.04 ML (filled squares, left axis) and relative binding energy (referenced to ΔE_{CO} on the original CO lattice) on CO lattices with different $\langle d_{CO} \rangle$ (open circles, right axis); (b) $\overline{\Delta E_{CO}}$ (eq 12) on Ru_{218} nanoparticles at three coverages for different numbers of desorbed CO. The solid lines in (a) denote the original CO lattice (open circle; structure, Figure 1e); curves represent the regression of Ru_{218} nanoparticle (gray) and lattice model (black) results to the functional form of eq 10.

$$P_1^{iso} = \left(\frac{1}{1 + K_{CO}[CO]}\right) \cdot \left(\frac{K_{CO}[CO]}{1 + K_{CO}[CO]}\right)^{\sigma_1} \quad (6)$$

where σ_1 is the number of contiguous sites (the coordination number of surface metal atoms; $\sigma_1 = 6$ for hexagonal close-packed (hcp) surfaces).

These treatments consider K_{CO} to be the same for all CO* and at all CO* (or coadsorbate) coverages, irrespective of the identity or the number of bound species at adjacent sites.[10,50−52] The assumption of quasi-equilibrated CO* coverages for a catalytic sequence at pseudo steady state ensures that the distribution of CO* remains random throughout the surface, because adsorption−desorption events occur much more frequently than the catalytic turnovers that consume CO* species.[9,10,20,25] Consequently, the probability of finding isolated ensembles with two (*and only two*) contiguous bare atoms is

$$P_2^{iso\_id} = \phi_2 \cdot \left(\frac{1}{1 + K_{CO}[CO]}\right)^2 \cdot \left(\frac{K_{CO}[CO]}{1 + K_{CO}[CO]}\right)^{\sigma_2} \quad (7)$$

The superscript "id" denotes the context of an ideal adlayer on which CO* binding properties are insensitive to the number of CO* at adjacent sites. ϕ_2 is a statistical coefficient that contains the coordination number of two-atom bare ensembles and the degeneracy factor that accounts for the overcounting of any given site pair. The values of ϕ_i (i = 3−6) depend on the specific arrangement of the bare atoms in such ensembles; they were derived recursively and also calculated using enumeration processes for the regular shapes specified in Table 1 for the hcp surfaces at (111) terraces of Ru_{218} particles (Figure 1). These ϕ_i values are shown for infinite surfaces in

https://doi.org/10.1021/jacs.4c07788
J. Am. Chem. Soc. 2024, 146, 22064−22076

Table 1 (and for finite surfaces in Supporting Information (SI)−S1). Surface planes other than hexagonal symmetry and any other spatial arrangements of bare atoms can be enumerated using the same procedures.

Similarly, the probability of finding isolated ensembles with n contiguous bare sites ($P_n^{\text{iso\_id}}$) is

$$P_n^{\text{iso\_id}} = \sum_j \left[\phi_{n,j} \cdot \left(\frac{1}{1 + K_{CO}[CO]} \right)^n \cdot \left(\frac{K_{CO}[CO]}{1 + K_{CO}[CO]} \right)^{\sigma_{n,j}} \right] \quad (8)$$

where the index j denotes a given shape of the n-atom bare ensemble (e.g., for n = 3, equilateral triangles, isosceles triangles, or lines), which sets the values of both $\phi_{n,j}$ and $\sigma_{n,j}$.

The assumption that K_{CO} remains insensitive to the occupancy of contiguous sites fails when coadsorbate interactions are important, as is the case of the crowded surfaces of practical catalysis. K_{CO} values increase with ensemble size because of the lower local coverages as bare ensembles grow and CO*−CO* repulsion weakens. Consequently, the binding and activity of CO* at the periphery of bare-site ensembles differ among different sizes and shapes for these ensembles, as examined next.

Figure 2a shows DFT-derived CO* binding energies (ΔE_{CO}, ZPE-corrected electronic energies), defined as

$$\Delta E_{CO} = E_{CO} + E_* - E_{CO*} \quad (9)$$

where E_{CO} is the energy of a gaseous CO molecule, E_* is the energy of Ru_{218} nanoparticle models after removing the center CO* at terraces, and E_{CO*} is the energy of Ru_{218} nanoparticles before any CO* desorption. These ΔE_{CO} values refer to CO* bound at the center of (111) terraces of Ru_{218} nanoparticles with 0.01, 1.00, and 1.04 ML of CO* (filled squares, Figure 2a), which lead, in turn, to different mean CO*−CO* distances ($\langle d_{CO} \rangle$; calculated as the mean C−C and O−O distances); small $\langle d_{CO} \rangle$ values correspond to high CO* coverages. ΔE_{CO} values decrease (binding weakens) with increasing CO* coverages (157 to 108 kJ mol^{-1} for 0.01 to 1.04 ML, respectively) because intermolecular repulsive interactions become stronger within denser adlayers; taken together with the stronger through-surface repulsion,[10,24,25] these interactions weaken CO* binding.

The intermolecular repulsion reflected in the effects of CO*−CO* distance can be described by an exponential relation between and $\langle d_{CO} \rangle$ (gray curve, Figure 2a; regressed parameters listed in SI−S2):

$$\Delta E_{CO} = \Delta E_{CO}^0 - \alpha \cdot \exp\left(-\frac{\langle d_{CO} \rangle}{\beta} \right) \quad (10)$$

where ΔE_{CO}^0 is the CO* binding energy at 0.01 ML (Figure 1a; in the absence of repulsive effects). α denotes the asymptotic value of the repulsive interactions as $\langle d_{CO} \rangle$ approaches zero and β describes the sensitivity of these interactions to $\langle d_{CO} \rangle$. This relationship illustrates an exponential decay of repulsion with increasing intermolecular distance, which has also been reported to describe the effects of adsorbate−adsorbate interactions among bound O-atoms on transition metal surfaces.[1,53]

These repulsive effects are also evident from lattice models that enable monotonic changes in CO* coverage (and $\langle d_{CO} \rangle$), instead of the discrete values imposed by the symmetry and finite size of nanoparticle models (Section 2). Such lattice models rigorously capture intermolecular repulsion but not the effects of through-surface interactions between Ru atoms and CO* molecules. The ΔE_{CO} values derived from lattice models with different $\langle d_{CO} \rangle$ values are reported using the initial value before contraction or expansion as the subtraction reference. These relative binding energies are accurately described by eq 10 (black curve, Figure 2a; regressed parameters, SI−S2), which become more negative as the CO* adlayers densify (open circles, Figure 2a), indicative of weaker binding as total CO* coverage increases. Relative binding energies become more sensitive to $\langle d_{CO} \rangle$ for higher initial coverages because of stronger repulsive interactions, as also shown by DFT-derived ΔE_{CO} values with increasing total CO* coverages on Ru_{218} nanoparticles (gray curve, Figure 2a).

Intermolecular repulsion on crowded surfaces destabilizes CO*, thus enabling its more facile desorption; desorption rates (r_{des}; per binding site) are proportional to the fractional CO* coverage (θ_{CO*}, eq 3):[20,25]

$$r_{des} = \frac{k_B T}{h} \exp\left(\frac{\Delta S_{des}^{\ddagger}}{k_B} \right) \exp\left(-\frac{\Delta H_{des}^{\ddagger}}{k_B T} \right) \cdot \theta_{CO*} \quad (11)$$

with the terms preceding θ_{CO*} denoting the desorption rate constant. Here, k_B is the Boltzmann constant, h is Planck's constant, and $\Delta S_{des}^{\ddagger}$ and $\Delta H_{des}^{\ddagger}$ are the activation entropy and enthalpy for CO desorption, respectively. The strong binding of CO* on Ru surfaces (108−157 kJ mol^{-1} for the center CO* on Ru_{218} models at 0.01−1.04 ML; Figure 2a) is accompanied by significant losses of translational and rotational freedom upon adsorption of CO molecules. Such entropy changes (S_{trans} + S_{rot}, eq 2), taken together with the ΔE_{CO} value from the 1.04 ML Ru_{218} model (108 kJ mol^{-1}, Figure 2a) as an estimate for $\Delta H_{des}^{\ddagger}$, lead to a r_{des} value of about 10^{14} s^{-1} at 573 K. Such desorption rates are much larger than measured CO_2−H_2 turnover rates (0.06−0.9 s^{-1}, 573 K, 1−25 kPa CO_2, 1−16 kPa H_2),[20] as is also the case for FTS reactions (0.02−0.4 s^{-1}, 573 K, 4−64 kPa CO, 2−280 kPa H_2)[10] on Ru/SiO_2, consistent with the assumption (and experimental confirmation) that CO adsorption−desorption steps are quasi-equilibrated during the catalytic sequences used here as illustrative examples.

Local CO* coverages decrease as desorption occurs, and bare surface ensembles form, leading to the local relaxation of CO*−CO* repulsion. This, in turn, causes stronger CO* binding at the periphery of bare ensembles. Figure 2b shows mean ΔE_{CO} values ($\overline{\Delta E_{CO}}$):

$$\overline{\Delta E_{CO}} = \frac{\Delta E_{CO_{total}}}{n} \quad (12)$$

as a function of the number of vicinal CO* removed (n, eq 12) from the center region of (111) terraces (dashed hexagon, Figure 1a) on Ru_{218} nanoparticles at three initial CO* coverages (before removing any CO*). Here, $\Delta E_{CO_{total}}$ is the energy required to desorb n contiguous CO* molecules from the (111) terrace (dashed hexagon, Figure 1a), with the n-atoms in a specific geometric arrangement displayed in Table 1. These geometries are constrained in this example to the terrace sites (dashed hexagon, Figure 1a) for illustrative purposes. These (more symmetric) ensemble geometries were chosen because their regular shapes and larger maximum inscribed circles are more conducive for accommodating typical molecular structures of intermediates and transition

https://doi.org/10.1021/jacs.4c07788
J. Am. Chem. Soc. 2024, 146, 22064−22076

Scheme 1. Schematic Depictions of Bare-Site Ensembles (Size 1−3) on Crowded Surfaces[a]

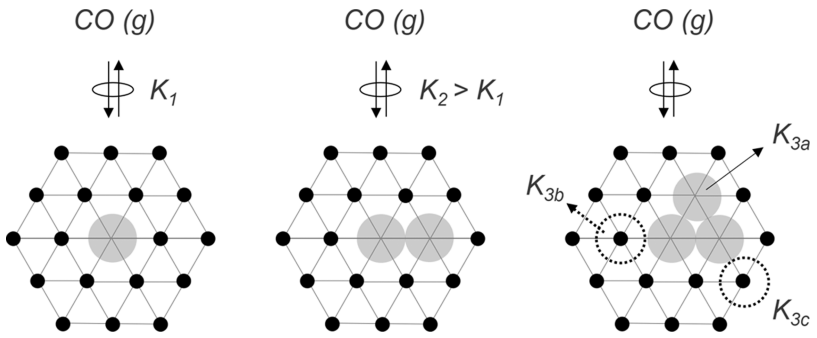

[a]Small black circles represent CO* and larger gray circles denote bare site(s) formed upon CO desorption. The dotted circles in the right panel indicate another two possible shapes of three-atom ensembles upon desorbing the circled CO* (lines and isosceles triangles).

states. A more exhaustive analysis of all other possible geometries represents an enumeration and a straightforward extension of the methods reported here. The value of $\overline{\Delta E_{CO}}$ (Figure 2b) represents the mean energy penalty incurred in removing each of the n CO* molecules to form the n-atom bare ensemble with the specified geometry.

The Ru_{218} nanoparticle with 0.01 ML of CO* exhibits no intermolecular repulsion because of the absence of vicinal CO* (Figure 1a). Consequently, CO* binding energies do not depend on the CO* coverage, leading to a constant $\overline{\Delta E_{CO}}$ value, namely that for the removal of the single CO* from the terrace center (Figure 2b). $\overline{\Delta E_{CO}}$ values increase as CO* species desorb from densely-covered surfaces (1.00 and 1.04 ML) and bare-site ensembles grow (Figure 2b), because CO*−CO* repulsion weakens as local CO* coverages decrease. These ensemble size effects on $\overline{\Delta E_{CO}}$ values are stronger at 1.04 than at 1.00 ML initial CO* coverages (Figure 2b), because repulsive interactions become stronger and more consequential for binding energies as adlayers densify (Figure 2a).

These trends in DFT-derived $\overline{\Delta E_{CO}}$ values with ensemble size (Figure 2b) and ΔE_{CO} values with $\langle d_{CO} \rangle$ (Figure 2a) illustrate the strong effects of ensemble size and total CO* coverages on CO* binding. Higher total CO* coverages cause stronger repulsion and weaken CO* binding; this weaker binding, however, is locally "dampened" around bare-site ensembles as they grow because of weaker repulsive interactions. Taken together, these two contrasting effects combine to determine the energy costs involved in desorbing contiguous CO* to create bare ensembles of a given size, in a manner that perturbs, as discussed next, the probability arguments that led to eqs 7 and 8 for the Langmuirian surfaces used to derive them.

3.2. Estimating the Probability of Forming Bare Landing Ensembles on Densely-Covered Surfaces. The values of ΔE_{CO} and K_{CO} on crowded surfaces increase as CO* is removed from contiguous sites to form bare ensembles and as the total CO* coverage decreases (Section 3.1). In such instances, the use of Langmuirian treatments (eq 7−8), which assume ΔE_{CO} and K_{CO} to remain constant with changes in total or local CO* coverages, becomes inaccurate in assessing the probability of finding bare-atom landing ensembles on densely-covered surfaces.

Scheme 1 depicts bare-site ensembles (size n = 1−3) on densely-covered Ru nanoparticle surfaces. The K_{CO} value for desorbing the first CO* (K_1; left panel, Scheme 1) senses intermolecular repulsion most strongly because local coverages are highest around the site from which CO* desorbs. The value of K_2 for desorbing a second CO* adjacent to the one-atom ensemble to form a two-atom ensemble (middle panel, Scheme 1) is larger than K_1 because the lower local CO* coverage weakens repulsion (Section 3.1). These effects cause P_n to become smaller than that for ideal surfaces, a trend that becomes increasingly evident as n increases.

The P_2 value for interacting CO* species for an isolated two-atom bare ensemble is given by

$$P_2^{iso} = \left(\frac{\phi_2}{(1 + K_1[CO])(1 + K_2[CO])}\right)\cdot\left(\frac{K_{3a}[CO]}{1 + K_{3a}[CO]}\right)^2\cdot \left(\frac{K_{3b}[CO]}{1 + K_{3b}[CO]}\right)^2\cdot\left(\frac{K_{3c}[CO]}{1 + K_{3c}[CO]}\right)^4 \quad (13)$$

where ϕ_2 is the statistical coefficient (Table 1), K_{3a} is the binding constant for the top (or bottom) CO* that forms an equilateral triangle with the vacancy pair (right panel, Scheme 1), K_{3b} accounts for the left (or right) CO* that forms a line, and K_{3c} is for the vertex CO* of isosceles triangles (right panel, Scheme 1). The last three multiplicative terms in eq 13 represent the probability that each of the eight sites adjacent to the two-atom bare ensemble is covered by CO*, a requirement for the vacancy pair to be isolated (instead of part of larger ensembles). This probability is assumed, without loss of generality, to be approximately given by equal values of K_{3a}, K_{3b}, and K_{3c} (taken as that for K_{3a}, which is required, in any case, to obtain P_3^{iso}; deviation <5%, SI−S3):

$$P_2^{iso} \approx \phi_2\cdot\frac{1}{1 + K_1[CO]}\cdot\frac{1}{1 + K_2[CO]}\cdot\left(\frac{K_{3a}[CO]}{1 + K_{3a}[CO]}\right)^8 \quad (14)$$

The analogous description (and approximation) for n-atom bare ensembles is

$$P_n^{iso} \approx \phi_n\cdot\prod_{i=1}^{n}\left(\frac{1}{1 + K_i[CO]}\right)\cdot\left(\frac{K_{n+1}[CO]}{1 + K_{n+1}[CO]}\right)^{\sigma_n} \quad (15)$$

where K_i denotes the desorption of the i^{th} CO* adjacent to ensembles of (i−1) bare atoms arranged in geometries specified in Table 1; σ_n is the number of contiguous sites for the n-atom bare ensemble. K_{n+1} is calculated for the contiguous site that must be vacated to form an n+1 ensemble and is used to represent binding constants for each of the σ_n CO* at the

https://doi.org/10.1021/jacs.4c07788
J. Am. Chem. Soc. 2024, 146, 22064−22076

periphery of the n-atom ensemble. This approximation maintains accuracy (≤5%; SI–S3) while circumventing the computational demands of calculating all K_{CO} values for the σ_n peripheral CO* molecules.

Figure 3 shows the probability (eq 15) that an infinite Ru(111) terrace with 1.00 ML of CO* (filled circles) and 1.04 ML of CO* (filled squares) will contain an ensemble of i bare atoms. The CO pressure ([CO] in eq 15) determines the density of CO* adlayers at each temperature (e.g., 500 K; derivations in SI–S2):

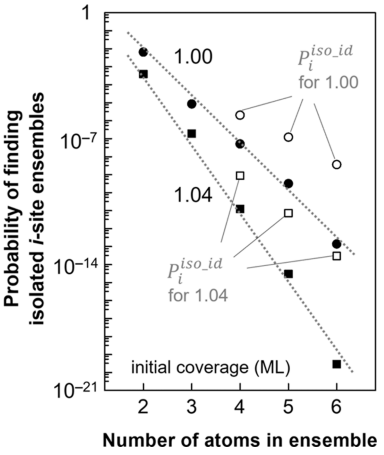

Figure 3. Probabilities (eq 15, 500 K) of finding i-site bare ensembles (i = 2–6) with given shapes (Table 1) on infinite Ru(111) terraces with 1.00 (filled circles) and 1.04 ML of CO* (filled squares). Probabilities derived by the noninteracting formalism ($P_i^{iso\_id}$, eq 8; 500 K) are also displayed (open symbols). Dotted lines denote trends.

$$\theta_{CO^*} = \frac{K_0 \cdot \exp\left(-\frac{\alpha}{RT} \cdot \exp\left(-\frac{\langle d_{CO}\rangle}{\beta}\right)\right) \cdot [CO]}{1 + K_0 \cdot \exp\left(-\frac{\alpha}{RT} \cdot \exp\left(-\frac{\langle d_{CO}\rangle}{\beta}\right)\right) \cdot [CO]} \quad (16)$$

where K_0 is the CO* binding constant on Ru_{218} models with 0.01 ML of CO* coverages (Figure 1a, 500 K). Equation 16 allows continuous assessments of the effects of the CO pressure (and temperature) on the CO* binding constants and fractional coverages on densely-covered Ru surfaces. Here, two specific CO pressures are discussed as illustrative examples; examinations of other conditions follow the same method described here. A CO pressure of 1 bar is assumed for the 1.04 ML model ($\langle d_{CO}\rangle$, 0.30 nm; Figure 1c), leading to a θ_{CO^*} value of 0.99 (eq 16; 500 K), consistent with its densely-covered surface (Figure 1c). A lower CO pressure of 0.12 kPa is derived from eq 16 (derivations in SI–S2) for the 1.00 ML model, a result of its less crowded surface ($\langle d_{CO}\rangle$, 0.31 nm; Figure 1b).

These probabilities (eq 15) decrease as ensemble size increases (i, 2 to 6; Figure 3) because of the greater energy penalty imposed by the removal of each additional CO* to form larger bare-atom ensembles. CO* binding energies increase with ensemble size (Figure 2b) as intermolecular repulsion locally weakens (lower local CO* coverages) and the remaining CO* species relax into more stable binding configurations. The contrasting tenets of Langmuirian models (noninteracting CO*; K_{CO} independent of coverage or ensemble size; eq 8) significantly overestimate the prevalence of larger ensembles at 1.00 and 1.04 ML of CO* (open symbols, Figure 3), the deviations of which become more consequential as CO* adlayers densify and as the ensemble size increases (disparity between filled and open symbols, Figure 3).

Larger ensembles are less prevalent than predicted from treatments that ignore intermolecular repulsion on densely-covered surfaces. They offer, however, greater stability benefits for kinetically-relevant transition states and their bound precursors through relieving local repulsion, which is not considered in Langmuirian treatments. Such energy costs and benefits, taken together, determine the kinetic competence of landing ensembles of a given size, as well as the extent to which ensembles of a given size contribute to turnover rates within a given sequence of elementary steps, as discussed next.

3.3. Assessing the Competence of Bare Ensembles for Stabilizing Transition States and Their Relevant Precursors. Bound species on crowded surfaces "sense" intermolecular repulsion from surrounding dense adlayers; the extent of repulsion depends on the overall surface coverage at the nanoparticle scale, but also locally on the number of CO* that is removed to form a given landing ensemble. Such effects

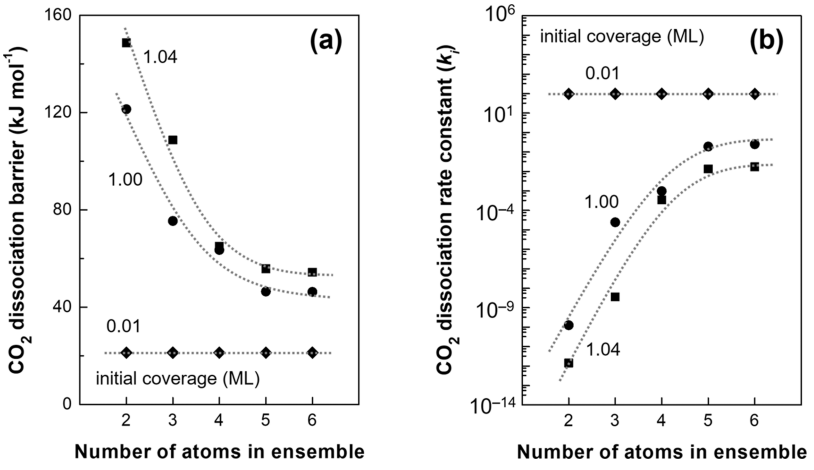

Figure 4. (a) DFT-derived barriers and (b) rate constants (k_i (bar^{-1} s^{-1}), 500 K; eq 18) for CO_2 dissociation (eq 17) on Ru_{218} nanoparticles with 0.01 (diamonds), 1.00 (circles), and 1.04 (squares) ML of CO* as a function of bare ensemble size (i = 2–6). Dotted lines and curves denote trends.

https://doi.org/10.1021/jacs.4c07788
J. Am. Chem. Soc. 2024, 146, 22064–22076

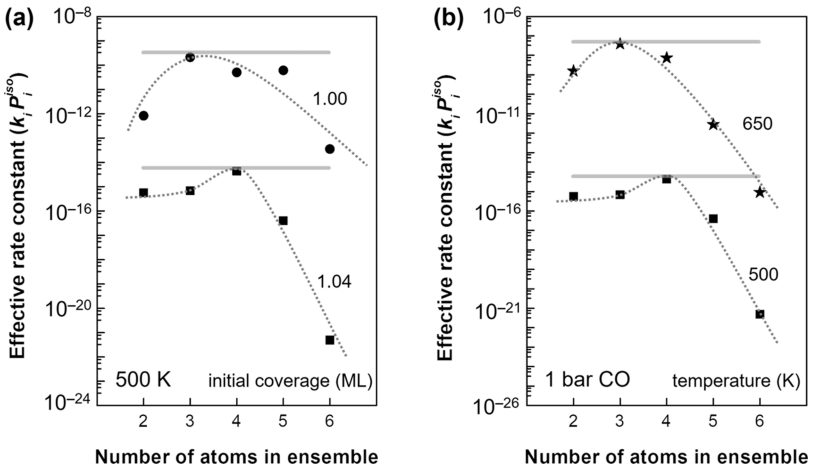

Figure 5. Effective rate constants ($k_i P_i^{iso}$ (bar^{-1} s^{-1}), eq 19) and total contributions from all ensemble sizes ($\sum_{i=2} k_i P_i^{iso}$, eq 20; horizontal lines) for CO_2 dissociation (eq 17) on Ru_{218} nanoparticles at (a) 500 K and different CO pressures [reflected by initial CO* coverages, 1.00 (circles) and 1.04 ML (squares)] and (b) 1 bar CO and different temperatures [500 K (squares) and 650 K (stars)]. The 500 K results in (b) are the same as those for 1.04 ML in (a), displayed for comparison. Dotted curves denote trends.

are evident from the energy requirements of removing each CO* for a given value of the total and local coverage (Figure 2). These coverages (at both scales) and the concomitant repulsive interactions also influence the stability of other bound species and specifically the kinetically-relevant transition states. Here, this is illustrated first for the $[CO-O]^{\ddagger}$ TS that mediates the dissociation of CO_2 to CO* and O*:

$$CO_2 + i^* \rightleftarrows [CO - O]^{\ddagger} \tag{17}$$

an elementary step involving interactions between a CO_2 molecule and a landing ensemble consisting of i contiguous bare metal atoms (i*).

Figure 4a shows DFT-derived CO_2 dissociation barriers (ZPE-corrected electronic energies) on landing ensembles ranging from two to six contiguous bare surface atoms on Ru_{218} nanoparticles at three total CO* coverages (CO_2 cannot land on a single site, as evident from bound structures that do not converge to a minimum energy; structure in Figure S6). These barriers represent the energy required to form the $[CO-O]^{\ddagger}$ TS from a gaseous CO_2 molecule and a Ru surface on which the i-atom landing ensemble was *already* created (by endothermic desorption of i contiguous CO*); they reflect the competence of bare ensembles of a given size in stabilizing the $[CO-O]^{\ddagger}$ TS, without considering the energy cost of their formation.

CO_2 dissociation activation barriers are very low at 0.01 ML of CO* coverages (21 kJ mol^{-1}, Figure 4a), as expected from the absence of repulsive interactions at such low CO* coverages and from the oxophilic character of bare Ru surfaces.[54,55] At such low CO* coverages, CO_2 dissociation barriers do not depend on the size of bare-atom ensembles (diamonds, Figure 4a) because such ensembles are not surrounded by a "detectable" number of CO* and remain unaware of the local coverage.

CO_2 dissociation barriers on two-site ensembles increase sharply (21 to 149 kJ mol^{-1}) as the coverage on Ru_{218} nanoparticles increases from 0.01 to 1.04 ML of CO* (Figure 4a) because of the destabilizing effects of repulsion by contiguous CO* adlayers on the $[CO-O]^{\ddagger}$ TS. Such repulsion also weakens the interactions between bound species and metal surfaces.[2−4,6,10] These weaker metal−TS interactions and the lateral repulsion from surrounding adlayers together cause the high DFT-derived CO_2 dissociation barriers observed on densely-covered Ru surfaces.

The formation of larger landing ensembles weakens local repulsion, thus rendering transition states more stable, but it also requires the endothermic desorption of a larger number of CO*. These larger spaces decrease the local "discomfort" of bound species, as evident for CO* molecules (Figure 2b), which become more strongly bound at the periphery of larger bare ensembles. Indeed, this is also the case for the $[CO-O]^{\ddagger}$ TS; its formation energy decreases monotonically (from 149 to 54 kJ mol^{-1}) as the landing ensemble grows (from 2 to 6; Figure 4a) on surfaces with 1.04 ML of CO*. Such effects of ensemble size are weaker at 1.00 ML of CO* coverages (121 to 46 mol^{-1} for i increasing from 2 to 6; Figure 4a) because repulsion is less severe at lower nanoparticle-scale CO* coverages (Section 3.2). These stabilizing benefits for the TS become less consequential for larger ensembles ($i \geq 4$, Figure 4a), because repulsive interactions between the $[CO-O]^{\ddagger}$ TS and CO* adlayers diminish when the TS binds on bare ensembles that are large enough to isolate it from the surrounding adlayers.

The corresponding rate constants (k_i, 500 K) for CO_2 dissociation steps (eq 17) can be estimated from activation enthalpies ($\Delta H_i^{\ddagger}$) and entropies ($\Delta S_i^{\ddagger}$):[46]

$$k_i = \frac{k_B T}{h} \exp\left(\frac{\Delta S_i^{\ddagger}}{k_B}\right) \exp\left(-\frac{\Delta H_i^{\ddagger}}{k_B T}\right) \tag{18}$$

These rate constants correspond to those for CO_2 dissociation steps on bare ensembles that have already been formed and thus solely reflect the kinetic competence of each ensemble in mediating CO_2 dissociation. The k_i values at 0.01 ML of CO* coverages are very large (97 bar^{-1} s^{-1}; $\geq 10^3$-fold larger than those at 1.04 ML; Figure 4b), consistent with their low CO_2 dissociation barriers (21 kJ mol^{-1}, Figure 4a). These k_i values are insensitive to ensemble size (i, 2−6; Figure 4b) because intermolecular repulsion is weak at such low coverages.

These k_i values are much smaller on more densely-covered surfaces ($\leq$0.25 bar^{-1} s^{-1} at 1.00 ML, $\leq$0.02 bar^{-1} s^{-1} at 1.04 ML; 500 K; Figure 4b) than on surfaces with 0.01 ML of CO*

https://doi.org/10.1021/jacs.4c07788
J. Am. Chem. Soc. 2024, 146, 22064−22076

coverages (97 bar^{-1} s^{-1}, 500 K; Figure 4b). The k_i trends with ensemble size reflect the lower CO_2 dissociation barriers and the concomitant greater stability of the $[CO-O]^{\ddagger}$ TS on larger ensembles (Figure 4a). The prevalence of a given ensemble, however, decreases as its size increases, especially within denser adlayers; such effects are stronger than expected from purely probabilistic arguments (Figure 3) because CO* binding becomes stronger at lower local coverages. Consequently, rigorous descriptions of the contributions of each ensemble to catalytic turnovers must consider the compensating effects of the less abundant large ensembles and their more competent stabilization of kinetically-relevant transition states.

The contribution from any i-atom bare ensemble to the CO_2 dissociation turnover rates is given by the product of the rate constant (k_i; eq 18), the probability of finding such ensembles (P_i^{iso}, eq 15), and the CO_2 pressure:

$$r_i = (k_i P_i^{iso}) \cdot [CO_2] \tag{19}$$

The effective rate constant ($k_i P_i^{iso}$) combines the competence and the prevalence of ensembles of a given size i, thus accounting for their kinetic contributions to CO_2 dissociation turnovers mediated by the $[CO-O]^{\ddagger}$ TS (eq 17). These $k_i P_i^{iso}$ values are larger at 1.00 ML (circles, Figure 5a) than at 1.04 ML of CO* coverages (squares, Figure 5a) for any given ensemble size (i = 2−6, Figure 5a), because stronger repulsion at higher CO* coverages decreases both the competence (k_i, Figure 4b) and the prevalence (P_i^{iso}, Figure 3) of each bare ensemble, irrespective of its size.

The maximum value of $k_i P_i^{iso}$ is reached on three-atom ensembles for 1.00 ML of CO* coverages and on four-atom ensembles for 1.04 ML of CO* coverages (Figure 5a). These effects of total CO* coverage on the optimal ensemble size arise from the different extents to which the $[CO-O]^{\ddagger}$ TS and the CO* molecules removed are destabilized by contiguous CO* adlayers. The benefits provided by optimal ensembles in stabilizing the $[CO-O]^{\ddagger}$ TS (by relieving local repulsion) compensate for the energy costs incurred upon the formation of such ensembles through the endothermic desorption of CO*. Denser CO* adlayers (1.04 vs 1.00 ML) and the consequent stronger repulsion destabilize both CO* (Figure 2a) and the $[CO-O]^{\ddagger}$ TS (Figure 4a) to a greater extent. This greater discomfort drives a preference for larger spaces so as to relax local repulsion and leads to larger optimal ensembles at 1.04 ML (four-atom, Figure 5a) than at 1.00 ML (three-atom, Figure 5a) of CO* coverages.

The probability of finding isolated bare ensembles of a given size at any nanoparticle-scale CO* coverage (P_i^{iso}, eq 15) and the rate constant that accounts for their CO_2 dissociation competence (k_i, Figure 4b) combine, after multiplying by the CO_2 pressure, to give the CO_2 dissociation turnover rate (r_{CO_2}) at that CO* coverage, which includes contributions from bare ensembles of all sizes:

$$r_{CO_2} = \left(\sum_{i=2} k_i P_i^{iso} \right) \cdot [CO_2] \tag{20}$$

These additive rate constants ($\sum_{i=2} k_i P_i^{iso}$; horizontal lines, Figure 5a) tend to reflect the predominant contributions from one specific ensemble (three-atom at 1.00 ML, four-atom at 1.04 ML). The size of these dominant ensembles depends on both the CO pressure and temperature because they dictate the density of CO* adlayers (eq 16) and, thus, the severity of repulsive interactions. The two densely-covered surfaces examined here (1.00 and 1.04 ML of CO*) correspond to two different CO pressures (0.12 kPa and 1 bar, respectively; Section 3.2) at a given temperature (500 K). Consequently, these results (three atoms at 1.00 ML, four atoms at 1.04 ML; Figure 5a) reflect the effects of the CO pressure, which determines nanoparticle-scale CO* coverages (eq 16). These coverages, as discussed above, influence the extent to which the $[CO-O]^{\ddagger}$ TS and the CO* molecules removed "sense" the prevalent severity of repulsion, thus dictating the size of dominant ensembles.

Higher temperatures lead to lower CO* coverages at any given CO pressure because of smaller K_{CO} values, which arise from their negative exponential dependence on T (eq 4). Consequently, these different CO* adlayer densities (1.00 and 1.04 ML) also correspond to two different temperatures at a given CO pressure (e.g., 1 bar). As an illustrative example, a reference temperature of 500 K is used for the 1.04 ML surface (Section 3.2); a higher temperature of 650 K is applied to the 1.00 ML model to account for its less densely-covered surface (1.00 vs 1.04 ML). This temperature (650 K) is derived from eq 16 in a manner similar to the derivation of the CO pressures (SI−S2). DFT-derived effective ($k_i P_i^{iso}$, eq 19; stars, Figure 5b) and additive ($\sum_{i=2} k_i P_i^{iso}$, eq 20; horizontal line, Figure 5b) rate constants at 650 K exhibit a smaller dominant ensemble (three-atom) than at 500 K (four-atom; squares, Figure 5b). These results indicate that higher temperatures, which lead to lower CO* coverages at a given CO pressure, reduce the areal requirement for large bare ensembles to alleviate local repulsion, analogous to the effects of lower CO pressures at a constant temperature (Figure 5a; 500 K).

The methods developed here to assess the size of the dominant ensemble and how it depends on nanoparticle-scale coverages (and on pressure and temperature) can also be applied to discern the kinetic relevance of specific elementary steps in a catalytic sequence and the relative contributions of parallel reaction channels to overall rates. The next section illustrates this strategy in determining the kinetic relevance of CO_2 dissociation and O*-removal steps and the relative contributions of direct and H-assisted CO_2 activation channels to CO_2−H_2 rates on Ru surfaces densely covered by CO*.

3.4. Kinetic Relevance of Elementary Steps and Parallel Reaction Channels on Densely-Covered Surfaces. The direct CO_2 dissociation step (to CO* and O*, Scheme 2) on Ru surfaces is quasi-equilibrated in CO_2−H_2 reactions, as evident from fast isotopic scrambling of

Scheme 2. Elementary Steps for Direct and H-Assisted CO_2 Activation Channels (to CO and H_2O)[a]

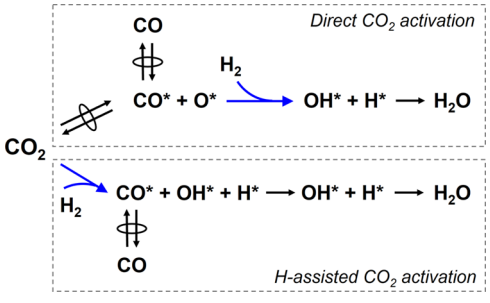

[a]Arrows with superimposed ovals denote quasi-equilibrated steps; arrows in blue denote kinetically-relevant steps.

https://doi.org/10.1021/jacs.4c07788
J. Am. Chem. Soc. 2024, 146, 22064−22076

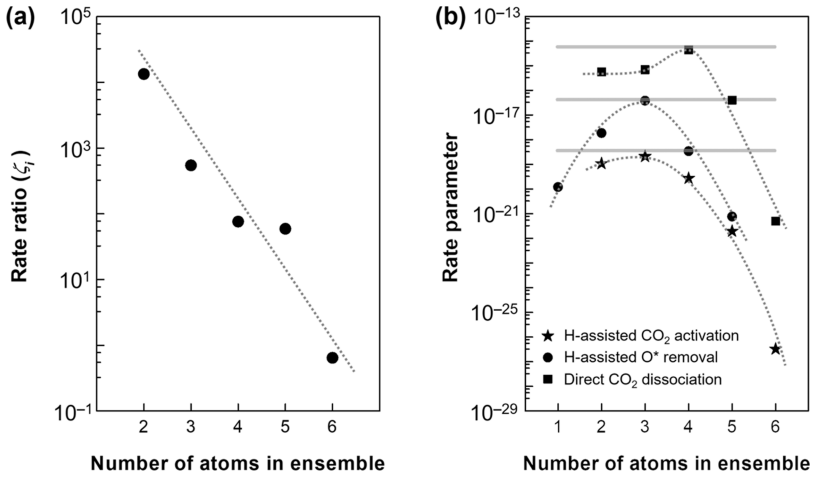

Figure 6. (a) Rate ratio (ζ_i, eq 26; 500 K, 1 bar CO, 1 bar H_2) and (b) rate parameters [squares, $k_i P_i^{iso}$ (bar^{-1} s^{-1}), eq 19, results from Figure 5a for comparison; circles, $k^i_{O-H}K^i_{disso}\sqrt{K_{H2}}P_i^{iso}$ ($bar^{-0.5}$ s^{-1}), eq 29; stars, $k^i_{CO-OH}\sqrt{K_{H2}}P_i^{iso}$ ($bar^{-1.5}$ s^{-1}), eq 32] and their additive contributions (horizontal lines; 500 K, 1 bar CO, 1 bar H_2) on Ru_{218} nanoparticles at 1.04 ML of CO*. Dotted lines and curves denote trends.

$C^{16}O_2$–$C^{18}O_2$–H_2 mixtures and kinetic trends with CO_2, H_2, and CO pressures on Ru nanoparticles densely covered by CO* (from in situ infrared spectra).[20] The subsequent O* removal by chemisorbed H atoms[20] acts as the sole kinetically-relevant step (Scheme 2) for CO_2 activation on such surfaces. The rate equations derived from these assumptions accurately capture measured kinetic trends for the rates of CO_2 conversion and CO and CH_4 formation.[20] This mechanistic proposal is considered next in the context of the ensemble-based method described in this study.

The O* formed via direct CO_2 dissociation (O^{i*}, i denotes the i-atom bare ensemble that stabilizes the $[CO-O]^{\ddagger}$ TS) can be consumed by either the reverse of direct CO_2 dissociation (O* reaction with a vicinal CO* to form CO_2 via the same $[CO-O]^{\ddagger}$ TS):

$$O^{i*} + CO^* \rightleftharpoons [CO-O]^{\ddagger} \tag{21}$$

or its reaction with a vicinal H* to form OH* (ultimately to H_2O) via a $[O-H]^{\ddagger}$ TS:

$$O^{i*} + H^* \rightleftharpoons [O-H]^{\ddagger} \tag{22}$$

The rate equations of these two steps are given by

$$r^i_{O-CO} = k^i_{O-CO}\cdot\theta_{O^{i*}}\cdot\theta_{CO^*} \tag{23}$$

$$r^i_{O-H} = k^i_{O-H}\cdot\theta_{O^{i*}}\cdot\theta_{H^*} \tag{24}$$

where k^i_{O-CO} is the rate constant for O* reaction with a vicinal CO* (eq 21) and k^i_{O-H} is that for O* reaction with a vicinal H* (eq 22). The θ_{H^*} term denotes the fractional H* coverage on CO*-covered Ru surfaces; these H* atoms bind at interstitial spaces within CO* adlayers rather than displacing CO* bound in atop configuration (Figure S7), consistent with previous DFT results on similar Ru surfaces.[10,24] DFT-derived small values of H_2 binding constants (K_{H2}; 1.6×10^{-7} to 1.7×10^{-5} bar^{-1} for i of 2–6 at 1.04 ML of CO*, 500 K) lead to very low magnitudes of θ_{H^*} at typical H_2 pressures (<0.005 at 1 bar H_2); such θ_{H^*} is given by (considering its interstitial binding):

$$\theta_{H^*} = \frac{\sqrt{K_{H2}}\cdot\sqrt{[H_2]}}{1+\sqrt{K_{H2}}\cdot\sqrt{[H_2]}} \approx \sqrt{K_{H2}[H_2]} \tag{25}$$

The quasi-equilibration of direct CO_2 dissociation (eq 17) requires that the reaction depicted by eq 21 proceeded at a much higher rate than that in eq 22. The ratio (ζ_i) of these two rates is given by

$$\zeta_i \equiv \frac{r^i_{O-CO}}{r^i_{O-H}} = \frac{k^i_{O-CO}\cdot\theta_{CO^*}}{k^i_{O-H}\cdot\sqrt{K_{H2}[H_2]}} \tag{26}$$

DFT-derived values of ζ_i (500 K, 1 bar CO, 1 bar H_2) on Ru_{218} nanoparticles at 1.04 ML of CO* are much greater than unity (60–10^4; Figure 6a) for ensembles with 2–5 bare atoms. The ζ_i value for the six-atom ensemble is smaller than unity (0.6, Figure 6a); this ensemble, however, does not contribute detectably to the overall turnover rates of either direct or H-assisted CO_2 activation channels (Figure 6b). Consequently, O* consumption by a vicinal CO* (eq 21) is much faster than by a vicinal H* (eq 22) at typical H_2 pressures (e.g., 1 bar), consistent with the mechanistic proposal of quasi-equilibrated CO_2 direct dissociation derived from experimental evidence.[20]

Quasi-equilibrated CO_2 dissociation and subsequent CO* adsorption–desorption steps (Scheme 2; Section 3.1) allow the two steps to be combined:

$$CO_2 + i^* \rightleftarrows CO + O^{i*} \tag{27}$$

to give O* fractional coverages ($\theta_{O^{i*}}$):

$$\theta_{O^{i*}} = K^i_{disso}P_i^{iso}\cdot\frac{[CO_2]}{[CO]} \tag{28}$$

K^i_{disso} is the combined equilibrium constant for CO_2 direct dissociation and CO* desorption on i-atom bare ensembles; P_i^{iso} (eq 15) is the probability of finding this isolated i-atom ensemble on densely-covered Ru surfaces (Section 3.2). This expression for $\theta_{O^{i*}}$ (eq 28) and the low prevalent coverages of H* (eq 25) allow the rate equation (eq 24) for the H-assisted O* removal step to be rewritten as

$$r^i_{O-H} = (k^i_{O-H}K^i_{disso}\sqrt{K_{H2}}P_i^{iso})\cdot\frac{[CO_2]\sqrt{[H_2]}}{[CO]} \tag{29}$$

The total reaction rate includes contributions from each bare ensemble:

https://doi.org/10.1021/jacs.4c07788
J. Am. Chem. Soc. 2024, 146, 22064–22076

$$r_{O-H} = \left(\sum_{i=1} k^i_{O-H} K^i_{disso} \sqrt{K_{H2}}\, P_i^{iso}\right) \cdot \frac{[CO_2]\sqrt{[H_2]}}{[CO]} \quad (30)$$

The DFT-derived $[O-H]^{\ddagger}$ TS can be isolated even on one-atom bare ensembles (structure in Figure S8), rendering these ensembles (i = 1) capable of mediating the H-assisted O* removal step. DFT-derived values of $k^i_{O-H} K^i_{disso} \sqrt{K_{H2}}\, P_i^{iso}$ (circles, Figure 6b; 500 K, 1 bar CO, 1 bar H_2) and additive contributions ($\sum_{i=1} k^i_{O-H} K^i_{disso} \sqrt{K_{H2}}\, P_i^{iso}$; horizontal line, Figure 6b) on Ru_{218} nanoparticles at 1.04 ML of CO* are much smaller ($k^i_{O-H} K^i_{disso} \sqrt{K_{H2}}\, P_i^{iso}$, 10−$10^4$-fold smaller; $\sum_{i=1} k^i_{O-H} K^i_{disso} \sqrt{K_{H2}}\, P_i^{iso}$, 100-fold smaller) than those for the direct CO_2 dissociation step (squares and horizontal line, Figure 6b; $k_i P_i^{iso}$ and $\sum_{i=2} k_i P_i^{iso}$, eq 20). These results indicate that H-assisted O* removal is significantly slower than direct CO_2 dissociation at typical H_2 pressures (e.g., 1 bar), leading to O* removal as the sole kinetically-relevant step for the direct CO_2 activation channel (Scheme 2), consistent with experiment-derived mechanistic proposals.[20]

Previous studies[26,54,55] have proposed CO_2 activation steps assisted by coadsorbed H-atoms (Scheme 2), forming CO* and OH* via a $[CO-OH]^{\ddagger}$ TS (i* denotes i-atom bare ensembles):

$$CO_2 + H^* + i^* \rightleftarrows [CO-OH]^{\ddagger} \quad (31)$$

at rates given by (for low H* coverages; eq 25):

$$r^i_{CO-OH} = (k^i_{CO-OH} \sqrt{K_{H2}}\, P_i^{iso}) \cdot [CO_2]\sqrt{[H_2]} \quad (32)$$

with k^i_{CO-OH} as the rate constant. The lumped rate parameter $k^i_{CO-OH} \sqrt{K_{H2}}\, P_i^{iso}$, by analogy with that for the direct CO_2 dissociation step ($k_i P_i^{iso}$, eq 19), accounts for the prevalence of isolated i-atom bare ensembles and for their competence in mediating H-assisted CO_2 activation steps (eq 31). These $k^i_{CO-OH} \sqrt{K_{H2}}\, P_i^{iso}$ values show a maximum for three-atom ensembles at 1.04 ML of CO* (stars, Figure 6b; 500 K, 1 bar CO, 1 bar H_2). The additive contribution (horizontal line, Figure 6b) from all bare ensembles

$$r_{CO-OH} = \left(\sum_{i=2} k^i_{CO-OH} \sqrt{K_{H2}}\, P_i^{iso}\right) \cdot [CO_2]\sqrt{[H_2]} \quad (33)$$

predominantly reflects the contributions from three-atom ensembles. This size, as discussed in Section 3.3, reflects the areal requirements of CO* and the $[CO-OH]^{\ddagger}$ TS and their tendency to interact with the (anti)solvating CO* adlayers.

The rate parameters for H-assisted CO_2 activation routes ($k^i_{CO-OH} \sqrt{K_{H2}}\, P_i^{iso}$, eq 32) are much smaller (rate parameters on each ensemble, 3−200-fold smaller; additive contributions, 100-fold smaller; Figure 6b) than for direct activation channels (circles and horizontal line, Figure 6b; 500 K, 1 bar CO, 1 bar H_2), for which O* removal by H* (eq 22) is the sole kinetically-relevant step. These results indicate that CO_2 molecules, after landing on Ru_{218} nanoparticle surfaces with 1.04 ML of CO*, will react preferentially via direct dissociation routes (eq 17) to form CO* and O*. This direct dissociation step is quasi-equilibrated (Figure 6a) and much faster than both subsequent O* removal by H* and parallel H-assisted CO_2 activation at typical conditions (e.g., 500 K, 1 bar H_2; Figure 6b), consistent with the mechanistic proposals derived from the measured CO_2, CO, and H_2 pressure effects and fast isotopic scrambling of $C^{16}O_2-C^{18}O_2-H_2$ mixtures during CO_2-H_2 reactions on dispersed Ru nanoparticles.[20] Assessments of other conditions (e.g., different temperatures and pressures) for these reaction steps represent a straightforward extension of the ensemble-based analysis described here, as shown above for the effects of the CO pressure and temperature on the rates of the direct CO_2 dissociation step (Figure 5).

This ensemble-based method, illustrated here by using the reduction of CO_2 to CO (and H_2O) on Ru nanoparticles at high CO* coverages, provides a general framework for assessing the contributions from any elementary steps on crowded metal surfaces. This framework dissects the analysis process into finding bare-site ensembles of a given size and subsequent assessments of their competence in stabilizing the TS. This treatment is essential to examine the kinetic relevance of elementary steps in a given catalytic sequence and to determine the contributions from parallel reaction channels at crowded surfaces that prevail in the practice of surface catalysis.

4. CONCLUSIONS

This study develops a general ensemble-based method that systematically assesses the effects of intermolecular repulsion on the kinetically-relevant TS and the most abundant bound species at crowded metal surfaces. This approach is illustrated by examining the relative contributions, kinetic relevance, and ensemble size requirements for two CO_2-H_2 routes (direct and H-assisted activation of CO_2 to CO and H_2O) on Ru nanoparticles densely covered by CO*. The method, however, is not restricted to specific bound species or reaction channels.

These treatments provide explicit insights into the consequences and chemical significance of repulsive interactions for surface catalysis within thermodynamically quasi-equilibrated systems. They offer a structured analytical framework for dissecting the dynamics of any elementary step on densely-covered surfaces into the probability of forming bare ensembles of a given size and their competence in stabilizing any given TS. This versatility underscores the broader applicability and significance of this ensemble-based approach in advancing the understanding of chemical dynamics of elementary steps at high coverages, a situation that prevails in catalytic practice.

■ ASSOCIATED CONTENT

Supporting Information

The Supporting Information is available free of charge at https://pubs.acs.org/doi/10.1021/jacs.4c07788.

Calculation details for the statistical coefficient ϕ_n; discussions on the coverage-dependent CO* binding energies; simplifications for probability calculations; structures for the "landing" of CO_2 on a single bare Ru atom; and structures for bound H-atoms and $[O-H]^{\ddagger}$ transition state on densely-covered Ru surfaces (PDF)

■ AUTHOR INFORMATION

Corresponding Author

Enrique Iglesia − *Department of Chemical and Biomolecular Engineering, University of California at Berkeley, Berkeley, California 94720, United States; Davidson School of*

Chemical Engineering, Purdue University, West Lafayette, Indiana 47907, United States; orcid.org/0000-0003-4109-1001; Email: iglesia@berkeley.edu, iglesia@purdue.edu

Author

Wenshuo Hu − *Department of Chemical and Biomolecular Engineering, University of California at Berkeley, Berkeley, California 94720, United States;* orcid.org/0000-0001-8280-1167

Complete contact information is available at: https://pubs.acs.org/10.1021/jacs.4c07788

Notes

The authors declare no competing financial interest.

■ ACKNOWLEDGMENTS

The authors thank Professor David Hibbitts at the University of Florida for technical discussions. Financial support from Exxon Mobil Corporation is gratefully acknowledged. This research used resources of the National Energy Research Scientific Computing Center (NERSC), a DOE Office of Science User Facility supported by the Office of Science of the U.S. Department of Energy under Contract No. DE-AC02-05CH11231 using NERSC award BES-ERCAP0021368, and resources at the Extreme Science and Engineering Discovery Environment (XSEDE), supported by the National Science Foundation (grant number ACI-1548562) under allocation CHM210014 and CHE200114. The authors also thank Drs. Mikalai Artsiusheuski and Karoline Kvande for proofreading the manuscript.

■ REFERENCES

(1) Goswami, A.; Ma, H.; Schneider, W. F. Consequences of adsorbate-adsorbate interactions for apparent kinetics of surface catalytic reactions. *J. Catal.* **2022**, *405*, 410−418.
(2) Piccinin, S.; Stamatakis, M. Steady-State CO Oxidation on Pd(111): First-Principles Kinetic Monte Carlo Simulations and Microkinetic Analysis. *Top. Catal.* **2017**, *60* (1−2), 141−151.
(3) García-Diéguez, M.; Iglesia, E. Structure sensitivity via decoration of low-coordination exposed metal atoms: CO oxidation catalysis on Pt clusters. *J. Catal.* **2013**, *301*, 198−209.
(4) Allian, A. D.; Takanabe, K.; Fujdala, K. L.; Hao, X.; Truex, T. J.; Cai, J.; Buda, C.; Neurock, M.; Iglesia, E. Chemisorption of CO and mechanism of CO oxidation on supported platinum nanoclusters. *J. Am. Chem. Soc.* **2011**, *133* (12), 4498−4517.
(5) Storsæter, S.; Chen, D.; Holmen, A. Microkinetic modelling of the formation of C1 and C2 products in the Fischer−Tropsch synthesis over cobalt catalysts. *Surf. Sci.* **2006**, *600* (10), 2051−2063.
(6) Stamatakis, M.; Piccinin, S. Rationalizing the Relation between Adlayer Structure and Observed Kinetics in Catalysis. *ACS Catal.* **2016**, *6* (3), 2105−2111.
(7) Mansour, H.; Iglesia, E. Theoretical and Experimental Assessments of Elementary Steps and Bound Intermediates in Catalytic H2−O2 Reactions on Dispersed Pt Nanoparticles. *J. Phys. Chem. C* **2023**, *127* (9), 4553−4569.
(8) Neurock, M.; Pallassana, V.; van Santen, R. A. The importance of transient states at higher coverages in catalytic reactions. *J. Am. Chem. Soc.* **2000**, *122* (6), 1150−1153.
(9) Iglesia, E.; Hibbitts, D. The Fischer−Tropsch synthesis: A few enduring mechanistic conundrums revisited. *J. Catal.* **2022**, *405*, 614−625.
(10) Liu, J.; Hibbitts, D.; Iglesia, E. Dense CO Adlayers as Enablers of CO Hydrogenation Turnovers on Ru Surfaces. *J. Am. Chem. Soc.* **2017**, *139* (34), 11789−11802.
(11) García-Diéguez, M.; Hibbitts, D. D.; Iglesia, E. Hydrogen Chemisorption Isotherms on Platinum Particles at Catalytic Temperatures: Langmuir and Two-Dimensional Gas Models Revisited. *J. Phys. Chem. C* **2019**, *123* (13), 8447−8462.
(12) Hellman, A.; Honkala, K. Including lateral interactions into microkinetic models of catalytic reactions. *J. Chem. Phys.* **2007**, *127* (19), No. 194704.
(13) Henrici-Olivé, G.; Olivé, S. The Fischer−Tropsch Synthesis: Molecular Weight Distribution of Primary Products and Reaction Mechanism. *Angew. Chem., Int. Ed.* **1976**, *15* (3), 136−141.
(14) Iglesia, E.; Soled, S. L.; Fiato, R. A. Fischer−Tropsch Synthesis on Cobalt and Ruthenium - Metal Dispersion and Support Effects on Reaction-Rate and Selectivity. *J. Catal.* **1992**, *137* (1), 212−224.
(15) Madon, R. J.; Iglesia, E. The Importance of Olefin Readsorption and H_2/CO Reactant Ratio for Hydrocarbon Chain Growth on Ruthenium Catalysts. *J. Catal.* **1993**, *139* (2), 576−590.
(16) Yang, J.; Ma, W.; Chen, D.; Holmen, A.; Davis, B. H. Fischer−Tropsch synthesis: A review of the effect of CO conversion on methane selectivity. *Appl. Catal., A* **2014**, *470*, 250−260.
(17) Nelson, N. C.; Nguyen, M. T.; Glezakou, V. A.; Rousseau, R.; Szanyi, J. Carboxyl intermediate formation via an in situ-generated metastable active site during water-gas shift catalysis. *Nat. Catal.* **2019**, *2* (10), 916−924.
(18) Dong, Z.; Nian, Y.; Liu, H.; Chen, J.; Wang, Y.; Wang, S.; Xu, J.; Han, Y.; Luo, L. Revealing synergetic structural activation of a CuAu surface during water-gas shift reaction. *Proc. Natl. Acad. Sci. U.S.A.* **2022**, *119* (23), No. e2120088119.
(19) Xin, H.; Lin, L.; Li, R.; Li, D.; Song, T.; Mu, R.; Fu, Q.; Bao, X. Overturning CO_2 Hydrogenation Selectivity with High Activity via Reaction-Induced Strong Metal-Support Interactions. *J. Am. Chem. Soc.* **2022**, *144* (11), 4874−4882.
(20) Mansour, H.; Iglesia, E. Mechanistic Connections between CO_2 and CO Hydrogenation on Dispersed Ruthenium Nanoparticles. *J. Am. Chem. Soc.* **2021**, *143* (30), 11582−11594.
(21) Zhou, C.; Asundi, A. S.; Goodman, E. D.; Hong, J.; Werghi, B.; Hoffman, A. S.; Nathan, S. S.; Bent, S. F.; Bare, S. R.; Cargnello, M. Steering CO_2 hydrogenation toward C-C coupling to hydrocarbons using porous organic polymer/metal interfaces. *Proc. Natl. Acad. Sci. U.S.A.* **2022**, *119* (7), No. e2114768119.
(22) Zhou, J.; Gao, Z.; Xiang, G.; Zhai, T.; Liu, Z.; Zhao, W.; Liang, X.; Wang, L. Interfacial compatibility critically controls Ru/TiO2 metal-support interaction modes in CO_2 hydrogenation. *Nat. Commun.* **2022**, *13* (1), No. 327.
(23) Park, E. D.; Lee, D.; Lee, H. C. Recent progress in selective CO removal in a H_2-rich stream. *Catal. Today* **2009**, *139* (4), 280−290.
(24) Hibbitts, D.; Dybeck, E.; Lawlor, T.; Neurock, M.; Iglesia, E. Preferential activation of CO near hydrocarbon chains during Fischer−Tropsch synthesis on Ru. *J. Catal.* **2016**, *337*, 91−101.
(25) Loveless, B. T.; Buda, C.; Neurock, M.; Iglesia, E. CO chemisorption and dissociation at high coverages during CO hydrogenation on Ru catalysts. *J. Am. Chem. Soc.* **2013**, *135* (16), 6107−6121.
(26) Ye, R. P.; Ding, J.; Gong, W.; Argyle, M. D.; Zhong, Q.; Wang, Y.; Russell, C. K.; Xu, Z.; Russell, A. G.; Li, Q.; Fan, M.; Yao, Y. G. CO_2 hydrogenation to high-value products via heterogeneous catalysis. *Nat. Commun.* **2019**, *10* (1), No. 5698.
(27) Zhdanov, V. P. Lattice-Gas Model of Bimolecular Reaction on Surface. *Surf. Sci.* **1981**, *102* (1), L35−L40.
(28) Zhdanov, V. P. Lattice-Gas Model for Description of the Adsorbed Molecules of two Kinds. *Surf. Sci.* **1981**, *111* (1), 63−79.
(29) Zhdanov, V. P. Effect of the Lateral Interaction of Adsorbed Molecules on Pre-Exponential Factor of the Desorption Rate-Constant. *Surf. Sci.* **1981**, *111* (1), L662−L666.
(30) Getman, R. B.; Schneider, W. F. DFT-Based Coverage-Dependent Model of Pt-Catalyzed NO Oxidation. *ChemCatChem* **2010**, *2* (11), 1450−1460.
(31) Lausche, A. C.; Medford, A. J.; Khan, T. S.; Xu, Y.; Bligaard, T.; Abild-Pedersen, F.; Norskov, J. K.; Studt, F. On the effect of coverage-

dependent adsorbate-adsorbate interactions for CO methanation on transition metal surfaces. *J. Catal.* **2013**, *307*, 275−282.
(32) Bajpai, A.; Frey, K.; Schneider, W. F. Comparison of Coverage-Dependent Binding Energy Models for Mean-Field Microkinetic Rate Predictions. *Langmuir* **2020**, *36* (1), 465−474.
(33) Chen, Z.; Wang, H.; Liu, Z.; Xu, X. Dynamic and Intermediate-Specific Local Coverage Controls the Syngas Conversion on Rh(111) Surfaces: An Operando Theoretical Analysis. *ACS Catal.* **2021**, *11* (7), 3830−3841.
(34) Pineda, M.; Stamatakis, M. Kinetic Monte Carlo simulations for heterogeneous catalysis: Fundamentals, current status, and challenges. *J. Chem. Phys.* **2022**, *156* (12), No. 120902.
(35) Liu, D.-J.; Evans, J. W. Realistic multisite lattice-gas modeling and KMC simulation of catalytic surface reactions: Kinetics and multiscale spatial behavior for CO-oxidation on metal (100) surfaces. *Prog. Surf. Sci.* **2013**, *88* (4), 393−521.
(36) Kresse, G.; Furthmuller, J. Efficient iterative schemes for ab initio total-energy calculations using a plane-wave basis set. *Phys. Rev. B* **1996**, *54* (16), 11169−11186.
(37) Perdew, J. P.; Burke, K.; Ernzerhof, M. Generalized gradient approximation made simple. *Phys. Rev. Lett.* **1996**, *77* (18), 3865−3868.
(38) Zhang, Y. K.; Yang, W. T. Comment on "Generalized gradient approximation made simple". *Phys. Rev. Lett.* **1998**, *80* (4), 890.
(39) Hammer, B.; Hansen, L. B.; Norskov, J. K. Improved adsorption energetics within density-functional theory using revised Perdew-Burke-Ernzerhof functionals. *Phys. Rev. B* **1999**, *59* (11), 7413−7421.
(40) Grimme, S.; Antony, J.; Ehrlich, S.; Krieg, H. A consistent and accurate ab initio parametrization of density functional dispersion correction (DFT-D) for the 94 elements H-Pu. *J. Chem. Phys.* **2010**, *132* (15), No. 154104.
(41) Grimme, S.; Ehrlich, S.; Goerigk, L. Effect of the damping function in dispersion corrected density functional theory. *J. Comput. Chem.* **2011**, *32* (7), 1456−1465.
(42) Blöchl, P. E. Projector augmented-wave method. *Phys. Rev. B* **1994**, *50* (24), 17953−17979.
(43) Kresse, G.; Joubert, D. From ultrasoft pseudopotentials to the projector augmented-wave method. *Phys. Rev. B* **1999**, *59* (3), 1758−1775.
(44) Chen, B. W. J.; Xu, L.; Mavrikakis, M. Computational Methods in Heterogeneous Catalysis. *Chem. Rev.* **2021**, *121* (2), 1007−1048.
(45) Abild-Pedersen, F.; Andersson, M. P. CO adsorption energies on metals with correction for high coordination adsorption sites − A density functional study. *Surf. Sci.* **2007**, *601* (7), 1747−1753.
(46) Cramer, C. J. *Essentials of Computational Chemistry: Theories and Models*, 2nd ed.; Wiley: Chichester, West Sussex, England; Hoboken, NJ, 2004; p 618.
(47) Henkelman, G.; Jonsson, H. Improved tangent estimate in the nudged elastic band method for finding minimum energy paths and saddle points. *J. Chem. Phys.* **2000**, *113* (22), 9978−9985.
(48) Henkelman, G.; Uberuaga, B. P.; Jonsson, H. A climbing image nudged elastic band method for finding saddle points and minimum energy paths. *J. Chem. Phys.* **2000**, *113* (22), 9901−9904.
(49) Henkelman, G.; Jonsson, H. A dimer method for finding saddle points on high dimensional potential surfaces using only first derivatives. *J. Chem. Phys.* **1999**, *111* (15), 7010−7022.
(50) Boudart, M.; Djéga-Mariadassou, G. *Kinetics of Heterogeneous Catalytic Reactions*; Princeton University Press: Princeton, NJ, 1984.
(51) Razdan, N. K.; Bhan, A. Kinetic description of site ensembles on catalytic surfaces. *Proc. Natl. Acad. Sci. U.S.A.* **2021**, *118* (8), No. e2019055118.
(52) Razdan, N. K.; Bhan, A. Catalytic site ensembles: A context to reexamine the Langmuir-Hinshelwood kinetic description. *J. Catal.* **2021**, *404*, 726−744.
(53) Frey, K.; Schmidt, D. J.; Wolverton, C.; Schneider, W. F. Implications of coverage-dependent O adsorption for catalytic NO oxidation on the late transition metals. *Catal. Sci. Technol.* **2014**, *4* (12), 4356−4365.
(54) Qi, Y.; Zhu, Y.-A.; Chen, D. Mechanism investigation and catalyst screening of high-temperature reverse water gas shift reaction. *Green Chem. Eng.* **2020**, *1* (2), 131−139.
(55) Dietz, L.; Piccinin, S.; Maestri, M. Mechanistic Insights into CO_2 Activation via Reverse Water−Gas Shift on Metal Surfaces. *J. Phys. Chem. C* **2015**, *119* (9), 4959−4966.

https://doi.org/10.1021/jacs.4c07788
J. Am. Chem. Soc. 2024, 146, 22064−22076